

# Electrochemical analysis of nanostructured iron oxides using cyclic voltammetry and scanning electrochemical microscopy

Heinz [Bülter](#)<sup>a</sup>

heinz.buelter@uni-oldenburg.de

Guy [Denuault](#)<sup>a, b, 1</sup>

gd@soton.ac.uk

Stefan [Mátéfi-Tempfli](#)<sup>a, c</sup>

stefan.matefi-tempfli@th-deg.de

Mária [Mátéfi-Tempfli](#)<sup>a</sup>

matefi\_tempfli@lycos.com

Carsten [Dosche](#)<sup>a, b, e</sup>

carsten.dosche@uni-oldenburg.de

Gunther [Wittstock](#)<sup>a, \*, 1</sup>

gunther.wittstock@uni-oldenburg.de

<sup>a</sup>Carl von Ossietzky University of Oldenburg, Department of Chemistry, D-26111 Oldenburg, Germany

<sup>b</sup>University of Southampton, Department of Chemistry, Highfield, Southampton, SO17 1BJ, UK

<sup>c</sup>Deggendorf Institute of Technology, Faculty of Natural Sciences and Industrial Engineering, European Campus Rottal-Inn, 84347 Pfarrkirchen, Germany

\*Corresponding author.

<sup>1</sup>ISE member.

---

## Abstract

Iron oxides in general and especially hematite,  $\alpha$ -Fe<sub>2</sub>O<sub>3</sub>, have become promising materials for the alkaline water electrolysis and photoelectrochemical water splitting, respectively. In the present study electrocatalytic electrodes with a thin film of  $\alpha$ -Fe<sub>2</sub>O<sub>3</sub> and with vertically aligned  $\alpha$ -Fe<sub>2</sub>O<sub>3</sub> nanowires were prepared. Cyclic voltammograms of the  $\alpha$ -Fe<sub>2</sub>O<sub>3</sub> nanowires revealed differences including a series of three unreported cathodic signals when compared to previously published voltammograms for polycrystalline iron oxides. The generation-collection mode of scanning electrochemical microscopy (SECM) using nanostructured Pt microdisc probes was exploited to detect soluble reaction products formed at the voltammetric peaks of the  $\alpha$ -Fe<sub>2</sub>O<sub>3</sub> electrode. SECM tip-substrate voltammetry unexpectedly showed that the reduction of Fe<sup>VI</sup> to Fe<sup>III</sup> on the cathodic sweep is accompanied by significant O<sub>2</sub> evolution.

---

**Keywords:** scanning electrochemical microscopy; nanostructured hematite electrodes; oxygen evolution reaction; alkaline water electrolysis

## 1 Introduction

Alkaline water electrolysis is a promising technology for H<sub>2</sub> production, a key step towards the development of a sustainable hydrogen economy [1-3]. The bottleneck of the electrolysis is the high overpotential required for the oxygen evolution reaction (OER) [4]. Consequently, research has focused on the development and characterization of improved electrocatalysts for the OER. Among them, iron oxides and especially hematite ( $\alpha$ -Fe<sub>2</sub>O<sub>3</sub>), have been considered as cheap and abundant catalysts for the OER [5]. Hematite is also a very promising material for photoelectrochemical water splitting [6,7]. Several strategies have been

investigated to increase the efficiency of the OER for example surface modifications [8], doping [9-11] and morphology control by nanostructuring [12,13]. In the present study, electrocatalysts were prepared as a thin film of  $\alpha$ -Fe<sub>2</sub>O<sub>3</sub> and as vertically aligned  $\alpha$ -Fe<sub>2</sub>O<sub>3</sub> nanowires.

Extensive work has been devoted to the electrochemistry of oxide-covered iron samples in various contexts. The behavior of such electrodes is complex due to the formation of passivating films, surface redox chemistry involving unusual oxidation states and interaction with ions and molecules from solution. For our work we build extensively on studies by Lyons et al. [14-17] and Joiret et al. [18]. A detailed account of these studies is given in the result and discussion section and is summarized in Table 1.

**Table 1** Peaks assignment for the Fe<sub>2</sub>O<sub>3,NW</sub> electrode and corresponding reference for polycrystalline iron [14-18,49-51,54], steel [52] and composite electrodes consisting of Fe<sub>2</sub>O<sub>3</sub> and exfoliated graphite [53].

alt-text: Table 1

Peak	$E_S/V^a$	Reported in Refs.	Assignment	Ref. for Assignm.
<b>A1</b>	-1.19	[14-16,18,50,51,53]	Fe <sup>I</sup> OH + OH <sup>-</sup> → Fe <sup>II</sup> (OH) <sub>2</sub> + e <sup>-</sup> (1) or Fe <sup>I</sup> OH + OH <sup>-</sup> → Fe <sup>II</sup> O + H <sub>2</sub> O + e <sup>-</sup> (2)	[14]
<b>A2</b>	-1.07	[14-18,49,51-53]	Fe <sup>II</sup> (OH) <sub>2</sub> + OH <sup>-</sup> → Fe <sup>III</sup> OOH + H <sub>2</sub> O + e <sup>-</sup> (3)	[17]
<b>A3</b>	+0.15	[16,18,54]	Fe <sup>III</sup> OOH + 3 OH <sup>-</sup> → Fe <sup>VI</sup> O <sub>3</sub> + 3e <sup>-</sup> + 2 H <sub>2</sub> O (4)	[54]
<b>C1</b>	-1.21	[16,18,52,53]	3 $\gamma$ -Fe <sup>III</sup> <sub>2</sub> O <sub>3</sub> + H <sub>2</sub> O + 2e <sup>-</sup> → 2 Fe <sup>III/II</sup> <sub>3</sub> O <sub>4</sub> + 2 OH <sup>-</sup> (5) 3 $\alpha$ -Fe <sup>III</sup> OOH + e <sup>-</sup> → Fe <sup>III/II</sup> <sub>3</sub> O <sub>4</sub> + H <sub>2</sub> O + OH <sup>-</sup> (6)	[18]
<b>C2</b>	-0.91	not reported		
<b>C3</b>	-0.58	not reported		
<b>C4</b>	-0.37	[16,18,54]	Fe <sup>VI</sup> O <sub>3</sub> + 3e <sup>-</sup> + 2 H <sub>2</sub> O → Fe <sup>III</sup> OOH + 3 OH <sup>-</sup> (7)	[54]
<b>C5</b>	+0.22	not reported		

<sup>a</sup> vs. SMSE as measured in this paper. Exact potential values vary between different reports.

The  $\alpha$ -Fe<sub>2</sub>O<sub>3</sub> electrodes were characterized by cyclic voltammetry (CV) and the tip-substrate voltammetry mode of scanning electrochemical microscopy (TSV-SECM). SECM has been used to study a wide range of interfacial processes at solid/liquid and liquid/liquid interfaces [19] including the corrosion of carbon steel or iron in alkaline and neutral media where the sample generation/tip collection mode (SG/TC) of SECM was applied to detect soluble Fe<sup>2+</sup> at the microelectrode (ME) which originated from the sample surface sites [20-24]. In addition, Cl<sup>-</sup> was generated at the ME to trigger pitting corrosion at the sample [23,25]. For SG/TC and feedback mode investigations of corrosion processes, several reversible redox mediators, e.g. ferrocenemethanol [26,27], [Fe(CN)<sub>6</sub>]<sup>3+</sup> [28] and I<sup>-</sup> [22,28,29] were added to the solution. Deliberate addition of mediators is controversial in corrosion studies as they may influence the corrosion behavior [30]. Therefore, several SECM corrosion studies [20,31-35] have exploited molecular oxygen O<sub>2</sub> naturally present in the solution. In the present paper we demonstrate how TSV-SECM using O<sub>2</sub> detection at nanostructured Pt MEs is applied to investigate and to identify redox processes from the complex voltammetric response of the electrocatalysts. Our approach also differs from the cited corrosion studies by the use of nanostructured Pt [36,37] as SECM probe. These MEs retain a disc-like geometry while offering a huge electroactive surface area which has been shown to promote the 4-electron reduction of oxygen [38] and the rapid oxidation and reduction of hydrogen peroxide [39]. As a result, the nanostructured microdiscs yield a stable and sensitive amperometric response ideal to perform long SECM experiments [40]. Here we have exploited the properties of the nanostructured Pt MEs to record small O<sub>2</sub> concentration changes and monitor the release of O<sub>2</sub> due to surface redox processes at  $\alpha$ -Fe<sub>2</sub>O<sub>3</sub> nanowires.

## 2 Experimental

### 2.1 Template and sample preparation

Samples were prepared in the form of *i*) films and *ii*) aligned nanowires. Both were supported by Au|Ti|SiO<sub>2</sub>|Si substrates prepared on one side of a thermally oxidized silicon wafer (100 cut, 100 nm SiO<sub>2</sub>). The nanowires were

formed by using anodic aluminium oxide (AAO) templates whose preparation has been detailed before [41,42]. The substrate was prepared by e-beam evaporation. A 100 nm thick layer of gold was deposited on a titanium adhesion layer to serve as an anodization barrier during electrochemical oxidation of the Al and also as a contacting electrode during anodization and further electrochemical growth of Fe nanowires or iron layers. For the formation of AAO templates a 1  $\mu\text{m}$  thick layer of Al was e-beam evaporated on the above described substrate using a similar Ti adhesion layer in between. Nanopores were formed in the Al layer on an area of 113  $\text{mm}^2$  by electrochemical oxidation at 40 V in 0.3 M oxalic acid at 4 °C. The formed pores were enlarged to the desired diameter by chemical etching in 0.5 M orthophosphoric acid at 30 °C [43]. Fe|Fe<sub>2</sub>O<sub>3</sub> films and nanowires were fabricated by pulsed electrodeposition of iron from an aerated acidic bath consisting of 120 g L<sup>-1</sup> FeSO<sub>4</sub>·7 H<sub>2</sub>O, 45 g L<sup>-1</sup> H<sub>3</sub>BO<sub>3</sub> and 1 g L<sup>-1</sup> citric acid at 30 °C with a platinum counter electrode and a saturated calomel reference electrode (SCE). The pulse cycle was 10 ms at -1.8 V vs. SCE and 90 ms at -0.8 V vs. SCE. The electrodeposition time was adjusted (typically 350 s) so that the Fe nanowire length reached about 1  $\mu\text{m}$ . After growing the nanowires, the AAO template was chemically removed in 2 M NaOH within 5 min under potentiostatic control at -0.8 V vs. SCE to protect the freshly formed Fe nanowires against oxidation and hydroxide formation. In order to keep the electrodes in contact with the solution, the procedure involved the successive gradual replacement of the plating bath with water, 2 M NaOH solution and again water. This approach was also used for the rinsing steps. The formation of a protective Fe<sub>2</sub>O<sub>3</sub> layer was initiated potentiostatically in pure water (300 s at 1.0 V vs. SCE). All potentials were chosen according to the Pourbaix potential-pH equilibrium diagram of the iron-water system [44]. Subsequently, the iron oxide layer thickness was increased to its final value by thermal oxidation in air at 300 °C.

## 2.2 Scanning electrochemical microscopy and cyclic voltammetry

The iron oxide electrodes were used as working electrodes and were mounted at the bottom of a cylindrical Teflon cell (8 mm diameter, 8 mm high) filled with 0.4 mL of 0.1 M NaOH (pro Analyti, Sigma Aldrich, Steinheim, Germany). The three-electrode cell was completed by a coiled Pt wire as auxiliary electrode and by a saturated mercurous sulfate electrode (SMSE) from EG&G (Princeton Applied Research, Oak Ridge, USA) connected via a salt bridge to the cell. All potentials are referenced to the SMSE. The experiments were conducted in a grounded and closed Faraday cage in the dark.

Disc-shaped MEs were prepared as probes for SECM by sealing a 25  $\mu\text{m}$  diameter Pt wire in glass and polishing the glass sheath so that its radius was typically 3 to 5 times larger than the radius  $r_T$  of the Pt microdisc. The face of the ME was polished to a mirror finish. To ensure a diffusion-controlled amperometric response for the reduction of dissolved O<sub>2</sub> and for the oxidation of HO<sub>2</sub><sup>-</sup>, the ME was modified with a ca. 2  $\mu\text{m}$  thick layer of nanostructured Pt prepared by electrodeposition of Pt within a lyotropic liquid crystal molecular template as previously reported [39,40]. The modified ME was mounted on a SECM instrument running under SECMx software [45]. The SECM used closed loop piezoelectric motors (mechONics AG, München, Germany) as positioning system and a CHI700 B bipotentiostat (CH Instruments, Austin TX, USA) [46]. An approach curve (ME current  $i_T$  versus microelectrode-sample distance  $d$ ) was recorded for vertical positioning while the ME reduced O<sub>2</sub> under steady state conditions with the substrate unbiased so that it would not consume or produce O<sub>2</sub>. The distance  $d$  was adjusted to 70  $\mu\text{m}$  and 10  $\mu\text{m}$  using the theoretical expression for hindered diffusion [47]. Afterwards, TSV-SECM [48] was used where the substrate current  $i_S$  and the ME current  $i_T$  were simultaneously recorded as function of the potential  $E_S$  applied to the iron oxide substrate electrode. The potential sweep was initiated from a value where no reaction occurred to one where the substrate produced or consumed oxygen. The cell was open to the atmosphere and the small background current at the ME due to the reduction of O<sub>2</sub> from the air-saturated electrolyte solution was used as a reference value.

## 2.3 Scanning electron microscopy

The physical shape of the nanowires was evaluated by scanning electron microscopy (SEM) using a FEI Helios NanoLab 600i DualBeam™ SEM/focused ion beam workstation (FEI, Hillsboro, OR, US) with a beam current of 86 pA and a voltage of 15 kV (Fig. 1a-c). The images were recorded in the field-free mode using an ICE detector with dwell times of either 10 or 30  $\mu\text{s}$  and a resolution of 1024 × 884 with a line integration value set to 4.

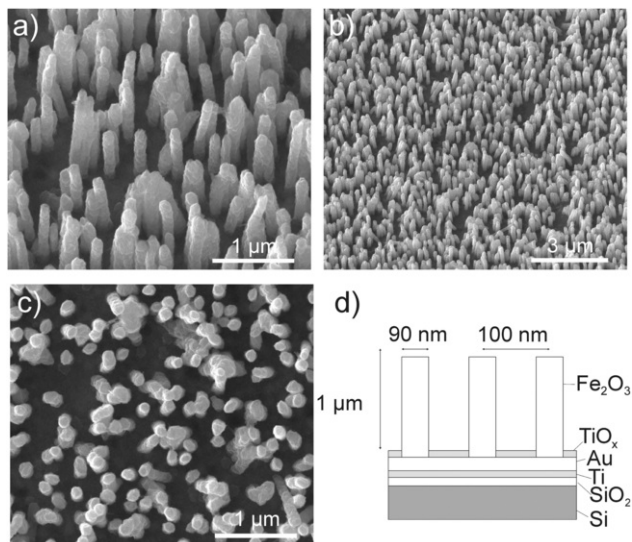


**Fig. 1** Dimensions of the iron oxide nanowires ( $\text{Fe}_2\text{O}_{3,\text{NW}}$ ) in a typical SEM micrographs of an array of nanowires tilted by  $30^\circ$ , (a and b), in top view (c) and as schematic (d).

alt-text: Fig. 1

## 3 Results and discussion

### 3.1 Structure of $\alpha\text{-Fe}_2\text{O}_3$ samples

The structural characterization of the vertically aligned  $\alpha\text{-Fe}_2\text{O}_3$  nanowires ( $\text{Fe}_2\text{O}_{3,\text{NW}}$ , Fig. 1) is provided as Supplementary Data in Appendix A. The dimensions of the layers and wires are given in Fig. 1d. X-ray diffraction on  $\text{Fe}_2\text{O}_{3,\text{NW}}$  shows peaks assigned to different crystallographic planes of  $\alpha\text{-Fe}_2\text{O}_3$  (Fig. S1). The physical shape of the vertically aligned nanowires was evaluated by scanning electron microscopy (Fig. 1a-c). High resolution photoelectron spectra confirm that assignment (Fig. S2).

### 3.2 Voltammetric response

Fig. 2a shows CVs of  $\text{Fe}_2\text{O}_{3,\text{NW}}$  at the beginning of experiments and after three days of interrupted experimentation. In general the shape of the CVs is characterized by a series of peaks, which result from surface redox processes. The oxygen evolution reaction (OER) and the oxygen reduction reaction (ORR) also affect the shape of the CV when  $E_s > 0.3$  V or  $E_s < -1.1$  V, respectively. At the beginning of experiments two anodic peaks **A1**, **A2** and one cathodic peak **C1** are present in the potential region of the ORR. These peaks have also been observed in CVs at similar potentials at iron oxide films [14-16,18,49-51], steel [52] and at composite electrodes of  $\text{Fe}_2\text{O}_3$  and exfoliated graphite [53]. Their assignment to specific reactions is summarized in Table 1.

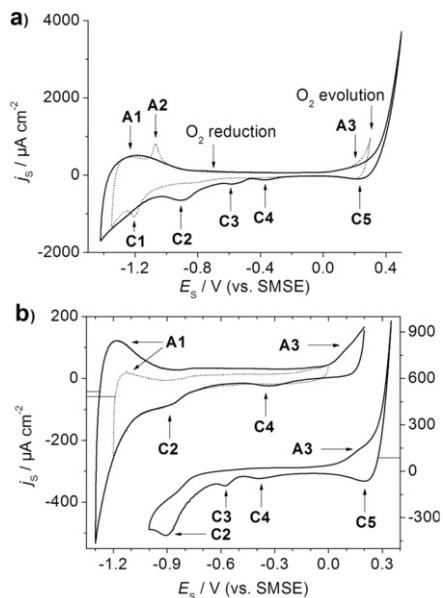


**Fig. 2** CVs in 0.1 M NaOH; (a) CVs of  $\text{Fe}_2\text{O}_{3,\text{NW}}$  at the beginning of experiments (dotted curve) and after three days of interrupted experimentation (solid curve) at  $100 \text{ mV s}^{-1}$ ; (b) Dependence of the peak shape on the upper vertex potential in the CV of  $\text{Fe}_2\text{O}_{3,\text{NW}}$  at  $50 \text{ mV s}^{-1}$ . The peaks **C4** and **A3** appear when the upper vertex potential is above  $E_\lambda > 0.0 \text{ V vs. SMSE}$  while **C3** and **C5** appear when  $E_\lambda > 0.3 \text{ V vs. SMSE}$ .

alt-text: Fig. 2

After interrupted cycling of the  $\text{Fe}_2\text{O}_{3,\text{NW}}$  electrodes between  $E_s = -1.42$  and  $0.50 \text{ V vs. SMSE}$  (Fig. 2a) over three days, the CV showed two anodic peaks **A1** and **A3** and four cathodic peaks **C2–C5**, i.e. the peaks **A2/C1** disappeared and the peaks **C2–C5** appeared. A comparison with literature data in Table 1 shows that the anodic peaks **A1–A3** and cathodic peaks **C1/C4** have been reported before for other oxide-covered iron samples. However, to the best of our knowledge, the peaks **C2**, **C3** and **C5** have not been reported for polycrystalline iron oxide.

Changes in peak heights and peak potentials have commonly been observed in the CVs of polycrystalline iron oxides upon ageing [14,49,55,56]. Thus, the changes observed in the CV of  $\text{Fe}_2\text{O}_{3,\text{NW}}$  are not surprising since electrode ageing changes the surface redox processes. Urbaniak et al. [53] reported for composite electrodes of  $\text{Fe}_2\text{O}_3$  and exfoliated graphite that peak **C1** appeared only in the first cycle and disappeared in the following cycles. In contrast, Xu et al. [52] and Lyons and Brandon [16] observed an increase of **C1** with electrode ageing for carbon steel and polycrystalline iron oxide, respectively. In case of polycrystalline iron oxide, the peak **C1** was only detected on one particular electrode [16] and **C1** is not a common feature in the CVs of polycrystalline iron oxide [14–16,18,51,56]. In our study the peak **C1** decreases and finally disappears with electrode ageing but in contrast to Xu et al. [52] the peak **C1** is seen over many cycles (Fig. 2a). Thus,  $\text{Fe}_2\text{O}_{3,\text{NW}}$  shows a particular behavior with respect to the peak **C1**.

Contrary to the disappearance of **A2** at  $\text{Fe}_2\text{O}_{3,\text{NW}}$  during potential cycling (Fig. 2a), the peak **A2** was reported to increase continuously with potential cycling for polycrystalline iron oxides [15–17,49,56]. It might be speculated, that the differences seen on  $\text{Fe}_2\text{O}_{3,\text{NW}}$  with respect to **C1** and **A2** at polycrystalline iron oxides [15–17,49,52,53,56] are linked to the appearance of **C2**, **C3**, **C5** because those signals have not been reported for polycrystalline iron oxide electrodes.

The corresponding pair **A3/C4** at  $\text{Fe}_2\text{O}_{3,\text{NW}}$  has occasionally been observed at polycrystalline iron oxides [16,18,54]. In 1985 Beck et al. [54] reported these peaks in very alkaline solutions of 40–50 mass-% of NaOH and KOH. Using CV and rotating iron disc electrodes, the peaks were assigned to the  $\text{Fe}^{\text{III}}/\text{Fe}^{\text{VI}}$  redox transition because of their experience with  $\text{Fe}^{\text{VI}}$  solutions and the correlation of potentials for the reduction of  $\text{Fe}^{\text{VI}}$  solution. Based on the Pourbaix diagram for iron [57–59] and the  $\text{Fe}^{\text{VI}}\text{O}_4^{2-}$  generation in alkaline media [60–62], Joiret et al. [18] similarly concluded that **A3/C4** originate from the  $\text{Fe}^{\text{III}}/\text{Fe}^{\text{VI}}$  redox transition. Both the stability of  $\text{Fe}^{\text{VI}}\text{O}_4^{2-}$  in alkaline media ( $\text{pH} \geq 10$ ) [63,64] and the tetrahedral structure of  $\text{Fe}^{\text{VI}}\text{O}_4^{2-}$  determined by X-ray diffraction [65] and Mössbauer spectroscopy [66] are known. Based on a potential-modulated reflectance study, Larramona and Guitérrez [51] concluded that  $\alpha\text{-Fe}_2\text{O}_3$  is oxidized to a soluble  $\text{Fe}^{\text{VI}}\text{O}_4^{2-}$  species in the potential region of **A3** in 1.0 M NaOH solution. The  $\text{Fe}^{\text{III}}/\text{Fe}^{\text{VI}}$  assignment is also supported by Lyons and Brandon [16] who speculated that the onset for the OER is related to the  $\text{Fe}^{\text{III}}/\text{Fe}^{\text{VI}}$  redox transition because the onset potential of the OER is similar to the peak potentials **A3/C4**. Thus, the  $\text{Fe}^{\text{VI}}$  species are likely to act as catalytic centers for the OER. A catalytic effect of  $\text{Fe}^{\text{VI}}\text{O}_4^{2-}$  on the OER was experimentally demonstrated [67]. Lyons and Brandon [16] remarked that it is an open question why **A3/C4** appear rarely. Despite the supposed importance for the OER, the assignment has not been completely clarified. They further

pointed out that the polycrystalline iron electrode that showed the pair **A3/C4** in its CV was apparently prepared in the same manner as other polycrystalline iron samples which did not produce this pair of peaks. Consequently, the reason for the appearance of **A3/C4** at specific single samples is currently unclear. Nevertheless, Lyons and Brandon [16] supposed that an unidentified aspect of electrode preparation induced the surface activation with respect to the  $\text{Fe}^{\text{III}}/\text{Fe}^{\text{VI}}$  redox transition. This general picture is confirmed by our investigations of films of  $\text{Fe}_2\text{O}_3$  prepared similarly to the  $\text{Fe}_2\text{O}_{3,\text{NW}}$  samples. Those samples showed comparable analytical characteristics (Fig. S3), but their CVs only showed a very small shoulder at the position of the peaks **A3/C4** after the same aging procedure (Fig. S4). This signal was too small for the planned TSV-SECM experiments and studies were continued with the  $\text{Fe}_2\text{O}_{3,\text{NW}}$  samples.

As noted by Lyons and Brandon [16], **A3/C4** are connected, because **C4** does not appear in the reverse sweep when the potential for **A3** is not reached in the forward sweep (Fig. 2b, dotted curve). In other words **A3/C4** appear in the CV of  $\text{Fe}_2\text{O}_{3,\text{NW}}$  only when the upper vertex potential  $E_\lambda > 0.0$  V vs. SMSE (Fig. 2b, upper solid curve). The appearance of the peaks **C3**, **C5** in the CV also depended on  $E_\lambda$ . When  $E_\lambda > 0.3$  V vs. SMSE, **C3** and **C5** appeared in the CV (Fig. 2b, lower solid curve). In contrast to **C3**, **C4** and **C5**, the peak **C2** was present in the CV even for  $E_\lambda = 0.0$  V vs. SMSE (Fig. 2b, dotted curve).

### 3.3 Peak assignment using TSV-SECM

The peak analysis was refined using TSV-SECM to detect species released from  $\text{Fe}_2\text{O}_{3,\text{NW}}$  into the solution at a specific  $E_s$  (Fig. 3d). The working distance between the SECM probe and the  $\text{Fe}_2\text{O}_{3,\text{NW}}$  substrate was set to 70  $\mu\text{m}$  and the corresponding diffusion time of  $\text{O}_2$  over that distance was estimated as 1.3 s with the method from Ref. [68]. The ME was polarized to a constant  $E_T = -1.0$  V vs. SMSE for diffusion-limited  $\text{O}_2$  detection. At such a large probe-substrate distance, the substrate hardly affects the diffusion of oxygen from the bulk and the tip current reaches a steady state which reflects the solubility and diffusion coefficient of oxygen, the number of electrons involved (4 because of the nanostructure [38]), the tip radius and the glass sheath thickness. The substrate CV was started at  $E_s = -0.1$  V vs. SMSE (Fig. 3d, black dot) and  $E_s$  was continuously increased at 1  $\text{mV s}^{-1}$ . The probe response clearly shows that  $\text{O}_2$  formation at  $\text{Fe}_2\text{O}_{3,\text{NW}}$  starts at circa  $E_s = +0.2$  V vs. SMSE and the reduction current  $i_T$  at the ME increases up to  $-24$  nA at  $E_{s,\lambda} = +0.35$  V vs. SMSE in the forward sweep. The increase of  $i_T$  demonstrates unequivocally the formation of molecular  $\text{O}_2$  at  $\text{Fe}_2\text{O}_{3,\text{NW}}$  for  $E_s > +0.2$  V because the ME is only sensitive to  $\text{O}_2$  (see Section 3.4). The ME current  $i_T$  does not reach its maximum at  $E_{s,\lambda} = +0.350$  V but at  $E_s = +0.339$  V in the reverse sweep because there is a delay between the maximum  $\text{O}_2$  formation rate at the sample and the highest reduction current at the ME due to the diffusional transport of  $\text{O}_2$  over the 70  $\mu\text{m}$  working distance between the  $\text{Fe}_2\text{O}_{3,\text{NW}}$  and the ME [68]. This delay of 11 s corresponds to 0.011 V at a scan rate of 1  $\text{mV s}^{-1}$ . Within the potential range of  $+0.2 < E_s/\text{V} < +0.4$  the SECM setup operates in the SG/TC mode (Fig. 3c) since  $\text{O}_2$  is generated at the  $\text{Fe}_2\text{O}_{3,\text{NW}}$  sample and collected at the ME. When  $E_s$  is decreased below  $E_s < +0.2$  V,  $i_T$  decreases because  $\text{O}_2$  formation at  $\text{Fe}_2\text{O}_{3,\text{NW}}$  stops and  $\text{O}_2$  in the solution between the  $\text{Fe}_2\text{O}_{3,\text{NW}}$  and the ME is slowly depleted by diffusion to the solution bulk and ongoing ORR at the ME. The ME current is lower than its value in the bulk (dotted line in Fig. 3d) because diffusion of oxygen is hindered (“negative feedback” in the SECM terminology) by the sample surface as illustrated in Fig. 3b. However,  $i_T$  drops quickly at  $E_s = -0.7$  V to almost 0 nA at  $E_s = -1.0$  V. The rapid decrease of  $i_T$  over these potentials is caused by the simultaneous  $\text{O}_2$  consumption at the  $\text{Fe}_2\text{O}_{3,\text{NW}}$  and the ME.  $\text{O}_2$  diffusing from the air-equilibrated solution bulk into the gap between the  $\text{Fe}_2\text{O}_{3,\text{NW}}$  and the ME is reduced at the  $\text{Fe}_2\text{O}_{3,\text{NW}}$  surface before reaching the ME (Fig. 3a). This situation, known as the redox competition mode, has been previously applied to detect ORR at samples with pulsed [69] and constant potentials [70]. After the inversion of the sweep direction,  $i_T$  starts to increase at ca.  $E_s = -0.9$  V because the ORR rate at the  $\text{Fe}_2\text{O}_{3,\text{NW}}$  decreases. Because  $\text{O}_2$  consumption at  $\text{Fe}_2\text{O}_{3,\text{NW}}$  occurs below ca.  $-0.7$  V and  $\text{O}_2$  generation begins above ca.  $E_s = 0.2$  V,  $\text{Fe}_2\text{O}_{3,\text{NW}}$  is supposed to neither consume nor generate  $\text{O}_2$  within these potential limits (Fig. 3b). Consequently, the current should follow the prediction for hindered diffusion (“negative feedback”) [47] because in this potential region the ME collects  $\text{O}_2$  diffusing from the solution bulk. In fact  $i_T$  is smaller than the ME ORR current in the bulk ( $-11.0$  nA) within  $-1.0 < E_s/\text{V} < 0.2$  because the diffusion of  $\text{O}_2$  to the ME is slightly hindered by the  $\text{Fe}_2\text{O}_{3,\text{NW}}$  surface at  $d = 70$   $\mu\text{m}$  and because  $\text{O}_2$  was depleted by ORR at the  $\text{Fe}_2\text{O}_{3,\text{NW}}$  sample in the preceding cycle.

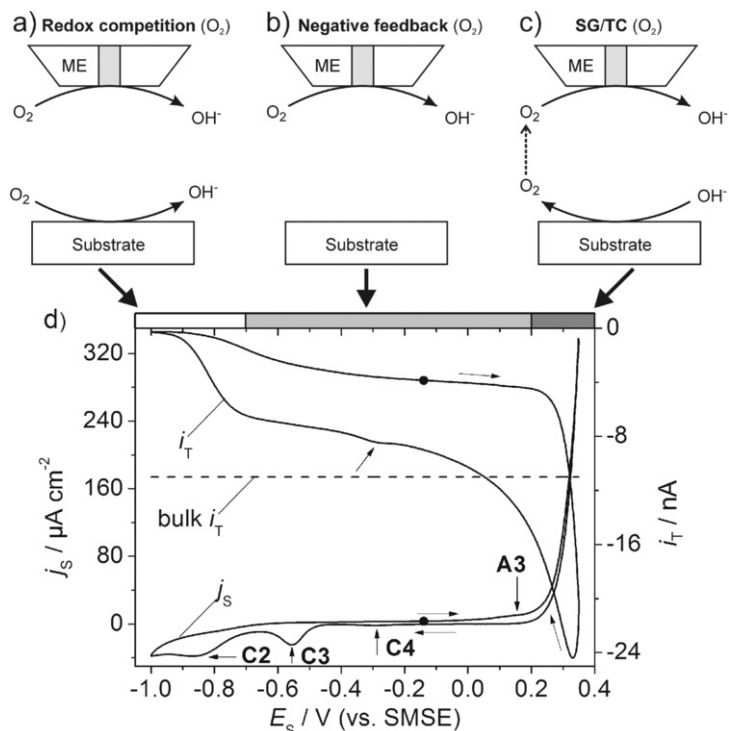


**Fig. 3** SECM operation modes and TSV-SECM above the  $\text{Fe}_2\text{O}_{3,\text{NW}}$  sample; (a) Redox competition mode with  $\text{O}_2$  consumption at both ME and  $\text{Fe}_2\text{O}_{3,\text{NW}}$ ; (b) Negative feedback mode with ORR at the ME only; (c) SG/TC mode with  $\text{O}_2$  generation at  $\text{Fe}_2\text{O}_{3,\text{NW}}$  and ORR at the ME; (d) TSV-SECM in 0.1 M NaOH with  $E_T = -1.0$  V vs. SMSE,  $d = 70$   $\mu\text{m}$  and  $v = 1$   $\text{mV s}^{-1}$ . The black dots indicate the start of the sweep. The operation modes relevant for the different potential regions are indicated on top of panel d.

alt-text: Fig. 3

A close inspection of the ME trace for the negative going potential sweep reveals a reproducible small increase of reduction currents during the reverse sweep at  $-0.3$  V (arrow in Fig. 3d). Because of the probe-substrate distance, there is a difference between the substrate potential  $E_S$  at which a peak in  $i_T$  is recorded and that at which the corresponding process at  $\text{Fe}_2\text{O}_{3,\text{NW}}$  occurs. Taking into account the time delay observed for the OER process (11 mV on the potential axis) the corresponding peak at  $\text{Fe}_2\text{O}_{3,\text{NW}}$  is **C4**. In order to increase the sensitivity for the peak analysis, the probe-substrate distance was decreased from 70 to 10  $\mu\text{m}$  and the scan rate was increased from 1 to 10  $\text{mV s}^{-1}$ . Fig. 4 shows the corresponding TSV-SECM data. During the reverse sweep  $i_T$  decreases and approaches the corresponding  $i_T$  values of the forward sweep for  $E_S < -0.1$  V. However, the ME reduction current increases significantly at  $E_S = -0.2$  V well within the potential range of peak **C4** at  $\text{Fe}_2\text{O}_{3,\text{NW}}$ . Within the range  $-0.4 < E_S / \text{V} < -0.2$ ,  $i_T$  reaches the maximum reduction current at  $E_S = -0.33$  V shortly after the maximum of **C4** at  $E_S = -0.30$  V. The shift between the extrema of ME and  $\text{Fe}_2\text{O}_{3,\text{NW}}$  currents (30 mV or 3 s) is caused by the time required for  $\text{O}_2$  to diffuse from  $\text{Fe}_2\text{O}_{3,\text{NW}}$  to the ME. Consequently, the detection of  $\text{O}_2$  by the ME proves that  $\text{O}_2$  is released from  $\text{Fe}_2\text{O}_{3,\text{NW}}$  during the process causing the signal **C4**. Since the redox processes corresponding to the peaks **C4/A3** are related [14,18,54,67], the TSV-SECM reveals that the  $\text{Fe}_2\text{O}_{3,\text{NW}}$  sample continuously evolves oxygen from  $+0.1$  V onwards, i.e. from the foot of peak **A3**, on the forward sweep and, unexpectedly, temporarily releases  $\text{O}_2$  at **C4** on the reverse sweep (Fig. 4). At **C4**, the OER has long stopped but the nanostructured ME is sufficiently sensitive to detect the release of oxygen from the sample surface. Our detection of  $\text{O}_2$  is in contrast to the conclusion of Joiret et al. [18] from their electrochemical quartz crystal microbalance data in which no mass change during **C4/A3** transitions were detected. Since a significant  $\text{O}_2$  release during **C4** was unequivocally detected in the present study, one might consider that the mass change in the experiments by Joiret et al. [18] was below the detection limit. Furthermore, the oxygen release might be masked by ion adsorption or formation of corrosion products. In the present study surface processes such as **A3/C4** are significantly enhanced by the large electroactive area resulting from the  $\text{Fe}_2\text{O}_3$  nanostructure.

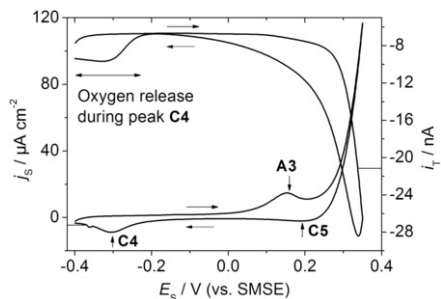


**Fig. 4** TSV-SECM of  $\text{Fe}_2\text{O}_3,\text{NW}$  in 0.1 M NaOH with  $E_T = -1.0$  V vs. SMSE,  $d = 10$   $\mu\text{m}$  and  $v = 10$   $\text{mV s}^{-1}$ .

alt-text: Fig. 4

The role of the soluble  $\text{Fe}^{\text{VI}}\text{O}_4^{2-}$  species as catalyst for the OER is not supported by Lyons and Brandon [14] since the  $\text{Fe}^{\text{VI}}$  species must be stabilized at the surface to act as catalytic centers for the OER. Furthermore, the finding of a linear dependency of the peak height of **C4** on the scan rate points towards a surface-bound  $\text{Fe}^{\text{VI}}$  species [54]. Consequently, insoluble complex anionic species such as  $[\text{Fe}^{\text{VI}}\text{O}_m(\text{OH})_n]^{p-}$  were considered as the catalytically active species [55]. Based on roughness factors obtained by the  $\text{OH}_{\text{ads}}$  desorption method, Lyons and Brandon [55] calculated that only a fraction of the geometric area of the oxide-covered Fe electrode is electrochemically active towards the OER. This result was explained by the notion that only a fraction of the surface  $\text{Fe}^{\text{VI}}$  species were stabilized by coordination with  $\text{OH}^-$  ions. Hence only a fraction of the  $\text{Fe}^{\text{VI}}$  species was able to catalyze the OER. Beck et al. [54] also distinguished between the  $\text{Fe}^{\text{VI}}\text{O}_4^{2-}$  in solution and their analogous surface species (formally written as  $\text{Fe}^{\text{VI}}\text{O}_3$ , Table 1, A3/C4).

The observations previously reported [16,18,54] and the clear finding of  $\text{O}_2$  release from the iron oxide sample in peak **C4** are consistent with peak **A3** reflecting the transition from  $\text{Fe}^{\text{III}}$  to  $\text{Fe}^{\text{VI}}$  as listed in Table 1. This process can be represented with the scheme shown below.



The iron centers at the surface may form peroxy species with two formal  $\text{Fe}^{\text{V}}$  centers. This would be a non-electrochemical reaction that does not require a specific potential. The resulting compound may chemically react further to  $\text{Fe}^{\text{IV}}$  centers under the release of molecular oxygen. If the potential is higher than the potential of peak **A3**, this species is immediately re-oxidized to the  $\text{Fe}^{\text{VI}}$  species and the catalytic cycle can start again. This cycle is at the heart of the OER and the dioxygen produced is easily detected by the ME when  $E_s > +0.2$  V. Alternatively, the peroxy species may transform to an adsorbed superoxide species with the Fe centers in the formal oxidation states IV and V. This reaction is independent of potential. The species will remain on the surface as long as the potential is below that of peak **A3** and above that of peak **C4**. The overall process is represented in Scheme 9.



The peak **C4** with the release of molecular oxygen would then be the reduction of the  $\text{Fe}^{\text{IV}}\text{-Fe}^{\text{V}}$  centers to  $\text{Fe}^{\text{III}}\text{-Fe}^{\text{III}}$  as shown below.



Peak **C3** is not explained yet. Given the variation of reported peak potentials for iron oxide samples and slight variations of experimental conditions, it might be possible that the reaction (7) in Table 1 refers to the peak **C3** in our study and peak **C4** is the reduction with oxygen release (10) that requires a preceding potential-independent surface reaction (9, right).

The position of the peak **C2** is remarkably close to the onset of ORR at  $\text{Fe}_2\text{O}_{3,\text{NW}}$  in Fig. 3d. It might be speculated that the Fe species responsible for peak **C2** catalyzes the ORR in the same way the higher-valent  $\text{Fe}^{\text{VI}}$  species catalyzes the OER.

### 3.4 Hydrogen peroxide formation

The interpretation of TSV-SECM data according to the processes described in Fig. 3a-c assumes that only  $\text{O}_2$  is detected at the ME. However, it is possible that  $\text{HO}_2^-$  is also generated by the electrocatalysts during the OER in alkaline media [71-73] (Fig. 5a). In such a case both  $\text{O}_2$  and  $\text{HO}_2^-$  would be reduced at  $E_T = -1.0$  V vs. SMSE and hence contribute to  $i_T$ . Therefore, it is important to assess whether dissolved peroxide species were involved in the TSV presented above. For this purpose the ME was approached to a distance  $d$  of 5-10  $\mu\text{m}$  above the  $\text{Fe}_2\text{O}_{3,\text{NW}}$  sample and polarized at  $E_T = 0.2$  V. At this potential only oxidation processes should occur and the ME response should be unaffected by the presence of dissolved oxygen. The ME current should primarily reflect the diffusion-controlled oxidation of  $\text{HO}_2^-$  and to a much lesser extent the oxidation of  $\text{OH}^-$  as schematically represented in (Fig. 5b). On Pt microdiscs the wave for  $\text{OH}^-$  oxidation appears at more positive potentials [74-76] but its contribution should not be neglected in view of the large bulk concentration of  $\text{OH}^-$ . The TSV-SECM data recorded with  $E_T = 0.2$  V shows no appreciable evidence for  $\text{HO}_2^-$  formation (Fig. 5c). If  $\text{HO}_2^-$  had been detected, the ME current would have increased when  $E_S$  was swept in the OER region. Instead  $i_T$  continuously decays throughout the forward sweep, undergoes an instantaneous drop of circa 50 pA upon reversal (thought to be linked to the double layer capacitance of the substrate via the bipotentiostat and the solution), then increases during the reverse sweep. The systematic drop in ME current observed when  $E_S > 0.1$  V and recovery when  $E_S < 0.1$  V can be understood in terms of the redox competition mode where both, ME and substrate, consume the same species, here  $\text{OH}^-$ . At the beginning of the sweep,  $i_T$  corresponds to the negative feedback mode due to hindered diffusion of  $\text{OH}^-$ . Above 0.1 V the substrate consumes  $\text{OH}^-$  and  $i_T$  decreases accordingly. At the end of the reverse sweep  $i_T$  does not quite recover its original value because of the gradual passivation of the ME due to oxide build-up. Frequent reconditioning is normally required to remove the oxide and to maintain a constant current for the oxidation of  $\text{OH}^-$  on oxide covered microdiscs [74,77].

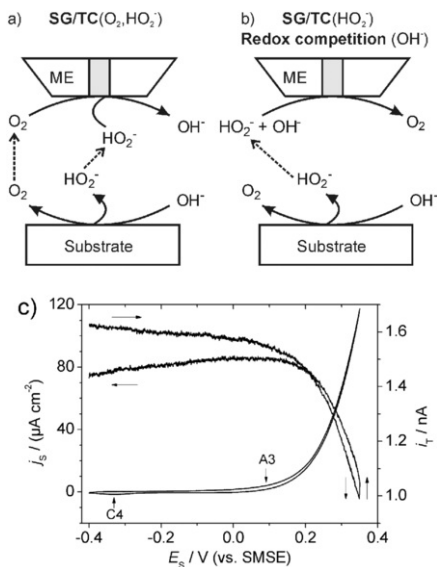


**Fig. 5** SECM operation modes for detection of possible  $\text{HO}_2^-$  formation at the substrate; (a)  $i_T$  increases due to  $\text{HO}_2^-$  reduction in addition to  $\text{O}_2$  reduction at the ME; (b) When the ME is polarized to a potential for  $\text{HO}_2^-$  oxidation,  $\text{HO}_2^-$  formation at the substrate can be unambiguously identified if  $\text{H}_2$  formation is thermodynamically excluded; (c) TSV-SECM of the  $\text{Fe}_2\text{O}_{3,\text{NW}}$  in 0.1 M NaOH with  $E_T = 0.2$  V vs. SMSE,  $d = 10$   $\mu\text{m}$  and  $v = 10$   $\text{mV s}^{-1}$ .

alt-text: Fig. 5

For comparison, a CV at the ME was recorded in a solution of 1 mM  $\text{H}_2\text{O}_2$  (Fig. S5). The nanostructured ME shows a stable diffusion-limited steady-state response for the oxidation of  $\text{H}_2\text{O}_2$ . In fact the reported detection limit of the nanostructured Pt ME for  $\text{H}_2\text{O}_2$  amounts to 4.5  $\mu\text{M}$  [39]. Overall, the results presented in Fig. 5 rule out the formation of peroxide species at the surface of the  $\text{Fe}_2\text{O}_{3,\text{NW}}$  sample and it is therefore clear that TSVs shown in Figs. 3d and 4 are solely due to the detection of dissolved oxygen and  $\text{HO}_2^-$  does not affect the ME response for the peak analysis in Section 3.3.

## 4 Conclusion

$\text{Fe}_2\text{O}_3$  nanowires show an electrochemical behavior remarkably different from  $\text{Fe}_2\text{O}_3$  films prepared in an analogous manner. Most signals found in cyclic voltammograms are in agreement with previous reports

about surface voltammetry of passivated iron samples of different origin. However, the peak pair **A3/C4** is always developing at the Fe<sub>2</sub>O<sub>3</sub> nanowires after continuous potential cycling while it is found only occasionally at other iron oxide samples [16,18,54]. Furthermore, Fe<sub>2</sub>O<sub>3</sub> nanowires showed a series of hitherto unreported peaks **C2**, **C3**, and **C5**. The investigation of the processes occurring at peak **C4** using TSV-SECM with nanoporous Pt ME allowed the unequivocal detection of O<sub>2</sub> released from the oxide layer. This process can be explained by the quasi-simultaneous release of O<sub>2</sub> occurring while Fe is electrochemically reduced from formal oxidation states Fe(V)-Fe(IV) to Fe(III)-Fe(III), Eq. (10).

## Acknowledgments

Guy Denuault and Stefan Mátéfi-Tempfli thank the Hanse-Wissenschaftskolleg, Institute for Advanced Study, Delmenhorst, Germany, for the award of a fellowship. Heinz Bültner gratefully acknowledges partial support by the graduate program of Energy Storage and Electromobility (GEENI). The assistance of Andrew Hector and Andreas Lesch is gratefully acknowledged.

## Appendix A. Supplementary data

Supplementary data about X-ray diffraction, scanning electron microscopy, X-ray photoelectron spectroscopy, cyclic voltammetry of Fe<sub>2</sub>O<sub>3</sub> films, and linear sweep voltammetry of the nanostructured Pt ME for H<sub>2</sub>O<sub>2</sub> oxidation and reduction in the online version, at <http://dx.doi.org/10.1016/j.electacta.2016.11.108>.

## References

- [1] J. Ohi, Hydrogen energy cycle: An overview, *J. Mater. Res.* **20**, 2005, 3180.
- [2] S. Marini, P. Salvi, P. Nelli, R. Pesenti, M. Villa, M. Berrettoni, G. Zangari and Y. Kiros, Advanced alkaline water electrolysis, *Electrochim. Acta* **82**, 2012, 384.
- [3] K. Zeng and D. Zhang, Recent progress in alkaline water electrolysis for hydrogen production and applications, *Prog. Energy Combust. Sci.* **36**, 2010, 307.
- [4] D.E. Hall, Nickel hydroxide (Ni(OH)<sub>2</sub>)-impregnated anodes for alkaline water electrolysis, *J. Electrochem. Soc.* **130**, 1983, 317.
- [5] M.P. Dare-Edwards, J.B. Goodenough, A. Hamnett and P.R. Trelvelick, Electrochemistry and photoelectrochemistry of iron(III) oxide, *J. Chem. Soc. Faraday Trans.* **1** (79), 1983, 2027.
- [6] J.H. Kennedy and K.W. Frese, Jr., Photooxidation of water at  $\alpha$ -iron(III) oxide electrodes, *J. Electrochem. Soc.* **125**, 1978, 709.
- [7] K. Sivula, F. Le Formal and M. Grätzel, Solar Water Splitting: Progress Using Hematite ( $\alpha$ -Fe<sub>2</sub>O<sub>3</sub>) Photoelectrodes, *ChemSusChem* **4**, 2011, 432.
- [8] S.D. Tilley, M. Cornuz, K. Sivula and M. Grätzel, Light-Induced Water Splitting with Hematite: Improved Nanostructure and Iridium Oxide Catalysis, *Angew. Chem. Int. Ed.* **49**, 2010, 6405.
- [9] N.T. Hahn and C.B. Mullins, Photoelectrochemical Performance of Nanostructured Ti- and Sn-Doped  $\alpha$ -Fe<sub>2</sub>O<sub>3</sub> Photoanodes, *Chem. Mater.* **22**, 2010, 6474.
- [10] I. Cesar, K. Sivula, A. Kay, R. Zboril and M. Grätzel, Influence of Feature Size Film Thickness and Silicon Doping on the Performance of Nanostructured Hematite Photoanodes for Solar Water Splitting, *J. Phys. Chem. C* **113**, 2009, 772.
- [11] M. Rioult, H. Magnan, D. Stanesco and A. Barbier, Single Crystalline Hematite Films for Solar Water Splitting: Ti-Doping and Thickness Effects, *J. Phys. Chem. C* **118**, 2014, 3007.
- [12] N. Beermann, L. Vayssieres, S.-E. Lindquist and A. Hagfeldt, Photoelectrochemical studies of oriented nanorod thin films of hematite, *J. Electrochem. Soc.* **147**, 2000, 2456.
- [13] S.K. Mohapatra, S.E. John, S. Banerjee and M. Misra, Water photooxidation by smooth and ultrathin  $\alpha$ -Fe<sub>2</sub>O<sub>3</sub> nanotube arrays, *Chem. Mater.* **21**, 2009, 3048.
- [14] M.E.G. Lyons, R.L. Doyle and M.P. Brandon, Redox switching and oxygen evolution at oxidized metal and metal oxide electrodes: iron in base, *Phys. Chem. Chem. Phys.* **13**, 2011, 21530.
- [15] L.D. Burke and M.E.G. Lyons, The formation and stability of hydrous oxide films on iron under potential cycling conditions in aqueous solution at high pH, *J. Electroanal. Chem.* **198**, 1986, 347.
- [16] M.E.G. Lyons and M.P. Brandon, Redox switching and oxygen evolution electrocatalysis in polymeric iron oxyhydroxide films, *Phys. Chem. Chem. Phys.* **11**, 2009, 2203.
- [17] R.L. Doyle and M.E.G. Lyons, Kinetics and mechanistic aspects of the oxygen evolution reaction at hydrous iron oxide films in base, *J. Electrochem. Soc.* **160**, 2013, H142.
- [18] S. Joiret, M. Keddou, X.R. Nóvoa, M.C. Pérez, C. Rangel and H. Takenouti, Use of EIS, ring-disk electrode, EQCM and Raman spectroscopy to study the film of oxides formed on iron in 1 M NaOH, *Cem. Concr.*

*Compos.* **24**, 2002, 7.

- [19] A.J. Bard and M.V. Mirkin, (Eds.), *Book Scanning Electrochemical Microscopy*, 2012, CRC Press Taylor & Francis Group Boca Raton; London, New York.
- [20] A.C. Bastos, A.M. Simoes, S. González, Y. González-García and R.M. Souto, Imaging concentration profiles of redox-active species in open-circuit corrosion processes with the scanning electrochemical microscope *Electrochem. Commun.* **6**, 2004, 1212.
- [21] Y. González-García, G.T. Burstein, S. González and R.M. Souto, Imaging metastable pits on austenitic stainless steel in situ at the open-circuit corrosion potential, *Electrochem. Commun.* **6**, 2004, 637.
- [22] Y. Yin, L. Niu, M. Lu, W. Guo and S. Chen, In situ characterization of localized corrosion of stainless steel by scanning electrochemical microscope, *Appl. Surf. Sci.* **255**, 2009, 9193.
- [23] J.W. Still and D.O. Wipf, Breakdown of the iron passive layer by use of the scanning electrochemical microscope, *J. Electrochem. Soc.* **144**, 1997, 2657.
- [24] E. Völker, C.G. Inchauspe and E.J. Calvo, Scanning electrochemical microscopy measurement of ferrous ion fluxes during localized corrosion of steel, *Electrochem. Commun.* **8**, 2006, 179.
- [25] C. Gabrielli, S. Joiret, M. Keddou, H. Perrot, N. Portail, P. Rousseau and V. Vivier, Development of a Coupled SECM-EQCM Technique for the Study of Pitting Corrosion on Iron, *J. Electrochem. Soc.* **153**, 2006, B68.
- [26] R.M. Souto, Y. Gonzalez-Garcia, S. Gonzalez and G.T. Burstein, Imaging the Origins of Coating Degradation and Blistering Caused by Electrolyte Immersion Assisted by SECM, *Electroanalysis* **21**, 2009, 2569.
- [27] Y. Xia, F. Cao, W. Liu, L. Chang and J. Zhang, The formation of passive films of carbon steel in borate buffer and their degradation behavior in NaCl solution by SECM, *Int. J. Electrochem. Sci.* **8**, 2013, 3057.
- [28] T.E. Lister and P.J. Pinhero, Microelectrode Array Microscopy: Investigation of Dynamic Behavior of Localized Corrosion at Type 304 Stainless Steel Surfaces, *Anal. Chem.* **77**, 2005, 2601.
- [29] T.E. Lister and P.J. Pinhero, The effect of localized electric fields on the detection of dissolved sulfur species from Type 304 stainless steel using scanning electrochemical microscopy, *Electrochim. Acta* **48**, 2003, 2371.
- [30] J.J. Santana, M. Paehler, W. Schuhmann and R.M. Souto, Investigation of Copper Corrosion Inhibition with Frequency-Dependent Alternating-Current Scanning Electrochemical Microscopy, *ChemPlusChem* **77**, 2012, 707.
- [31] R.M. Souto, Y. Gonzalez-Garcia and S. Gonzalez, Characterization of coating systems by scanning electrochemical microscopy: Surface topology and blistering, *Prog. Org. Coat.* **65**, 2009, 435.
- [32] R.M. Souto, L. Fernandez-Merida and S. Gonzalez, SECM Imaging of Interfacial Processes in Defective Organic Coatings Applied on Metallic Substrates Using Oxygen as Redox Mediator, *Electroanalysis* **21**, 2009, 2640.
- [33] J. Izquierdo, L. Nagy, A. Varga, J.J. Santana, G. Nagy and R.M. Souto, Spatially resolved measurement of electrochemical activity and pH distributions in corrosion processes by scanning electrochemical microscopy using antimony microelectrode tips, *Electrochim. Acta* **56**, 2011, 8846.
- [34] R. Leiva-Garcia, R. Akid, D. Greenfield, J. Gittens, M.J. Munoz-Portero and J. Garcia-Anton, Study of the sensitisation of a highly alloyed austenitic stainless steel Alloy 926 (UNS N08926), by means of scanning electrochemical microscopy, *Electrochim. Acta* **70**, 2012, 105.
- [35] J.J. Santana, J. Gonzalez-Guzman, L. Fernandez-Merida, S. Gonzalez and R.M. Souto, Visualization of local degradation processes in coated metals by means of scanning electrochemical microscopy in the redox competition mode, *Electrochim. Acta* **55**, 2010, 4488.
- [36] J.M. Elliott, P.R. Birkin, P.N. Bartlett and G.S. Attard, Platinum Microelectrodes with Unique High Surface Areas, *Langmuir* **15**, 1999, 7411.
- [37] G.S. Attard, P.N. Bartlett, N.R.B. Coleman, J.M. Elliott, J.R. Owen and J.H. Wang, Mesoporous platinum films from lyotropic liquid crystalline phases, *Science* **278**, 1997, 838.
- [38] P.R. Birkin, J.M. Elliott and Y.E. Watson, Electrochemical reduction of oxygen on mesoporous platinum microelectrodes, *Chem. Commun.* 2000, 1693.
- [39] S.A.G. Evans, J.M. Elliott, L.M. Andrews, P.N. Bartlett, P.J. Doyle and G. Denuault, Detection of hydrogen peroxide at mesoporous platinum microelectrodes, *Anal. Chem.* **74**, 2002, 1322.
- [40] S.A.G. Evans, K. Brakha, M. Billon, P. Mailley and G. Denuault, Scanning electrochemical microscopy (SECM): localized glucose oxidase immobilization via the direct electrochemical microspotting of polypyrrole-

biotin films, *Electrochem. Commun.* **7**, 2005, 135.

- [41] S. Mátéfi-Tempfli, M. Mátéfi-Tempfli, A. Vlad, V. Antohe and L. Piraux, Nanowires and nanostructures fabrication using template methods: a step forward to real devices combining electrochemical synthesis with lithographic techniques, *J. Mater. Sci.: Mater. Electron.* **20**, 2009, 249.
- [42] S. Mátéfi-Tempfli, Nanostructures Grown Via Electrochemical Template Methods: Synthesis, Measurements and Applications, In: E.D. Carlson, (Ed), *Encyclopedia of Nanotechnology*, 2009, Nova Science Publishers Inc, 459.
- [43] A. Vlad, M. Mátéfi-Tempfli, S. Faniel, V. Bayot, S. Melinte, L. Piraux and S. Mátéfi-Tempfli, Controlled growth of single nanowires within a supported alumina template, *Nanotechnology* **17**, 2006, 4873.
- [44] M. Pourbaix, Atlas of Electrochemical Equilibria in Aqueous Solutions, 1974, National Association of Corrosion Engineers (NACE) and Centre Belge d'Etude de la Corrosion (CEBELCOR); Houston.
- [45] C. Nunes Kirchner, K.H. Hallmeier, R. Szargan, T. Raschke, C. Radehaus and G. Wittstock, Evaluation of Thin Film Titanium Nitride Electrodes for Electroanalytical Applications, *Electroanalysis* **19**, 2007, 1023.
- [46] W. Nogala, K. Szot, M. Burchardt, F. Roelfs, J. Rogalski, M. Opallo and G. Wittstock, Feedback mode SECM study of laccase and bilirubin oxidase immobilised in a sol-gel processed silicate film, *Analyst* **135**, 2010, 2051.
- [47] R. Cornut and C. Lefrou, New analytical approximations for negative feedback currents with a microdisk SECM tip, *J. Electroanal. Chem.* **608**, 2007, 59.
- [48] G. Denuault, M.H.T. Frank and L.M. Peter, Scanning Electrochemical Microscopy: Potentiometric Probing of Ion Fluxes, *Faraday Discuss.* **94**, 1992, 23.
- [49] S. Juanto, R.S. Schrebler, J.O. Zerbino, J.R. Vilche and A.J. Arvia, The influence of different cations on the electrochemical and ellipsometric behaviour of iron in alkaline media, *Electrochim. Acta* **36**, 1991, 1143.
- [50] L. Freire, X.R. Nóvoa, M.F. Montemor and M.J. Carmezim, Study of passive films formed on mild steel in alkaline media by the application of anodic potentials, *Mater. Chem. Phys.* **114**, 2009, 962.
- [51] G. Larramona and C. Gutiérrez, The passive film on iron at pH 1-14. A potential-modulated reflectance study, *J. Electrochem. Soc.* **136**, 1989, 2171.
- [52] W. Xu, K. Daub, X. Zhang, J.J. Noel, D.W. Shoesmith and J.C. Wren, Oxide formation and conversion on carbon steel in mildly basic solutions, *Electrochimica Acta* **54**, 2009, 5727.
- [53] J. Urbaniak, J.M. Skowronski and B. Olejnik, Preparation of Fe<sub>2</sub>O<sub>3</sub>-exfoliated graphite composite and its electrochemical properties investigated in alkaline solution, *Journal of Solid State Electrochemistry* **14**, 2010, 1629.
- [54] F. Beck, R. Kaus and M. Oberst, Transpassive dissolution of iron to ferrate(VI) in concentrated alkali [metal] hydroxide solutions, *Electrochim. Acta* **30**, 1985, 173.
- [55] M.E.G. Lyons and M.P. Brandon, The oxygen evolution reaction on passive oxide covered transition metal electrodes in alkaline solution. Part III - iron, *Int. J. Electrochem. Sci.* **3**, 2008, 1463.
- [56] M.E.G. Lyons and M.P. Brandon, A comparative study of the oxygen evolution reaction on oxidized nickel, cobalt and iron electrodes in base, *J. Electroanal. Chem.* **641**, 2010, 119.
- [57] R.W. Revie and H.H. Uhlig, *Corrosion and Corrosion Control*, 2008, Wiley; Hoboken New Jersey.
- [58] G. Wulfsberg, *Inorganic Chemistry*, 2000, University Science Books; Sausalita California.
- [59] B. Beverskog and I. Puigdomenech, Revised Pourbaix diagrams for iron at 25-300 °C, *Corros. Sci.* **38**, 1996, 2121.
- [60] K. Bouzek and I. Rousar, Influence of anode material on current yields during ferrate(VI) production by anodic iron dissolution. Part I. Current efficiency during anodic dissolution of gray cast iron to ferrate(VI) in concentrated alkali [metal] hydroxide solutions, *J. Appl. Electrochem.* **26**, 1996, 919.
- [61] K. Bouzek, I. Rousar and M.A. Taylor, Influence of anode material on current yield during ferrate(VI) production by anodic iron dissolution. Part II: current efficiency during anodic dissolution of white cast iron to ferrate(VI) in concentrated alkali hydroxide solutions, *J. Appl. Electrochem.* **26**, 1996, 925.
- [62] Z. Macova, K. Bouzek, J. Hives, V.K. Sharma, R.J. Terryn and J.C. Baum, Research progress in the electrochemical synthesis of ferrate(VI), *Electrochim. Acta* **54**, 2009, 2673.

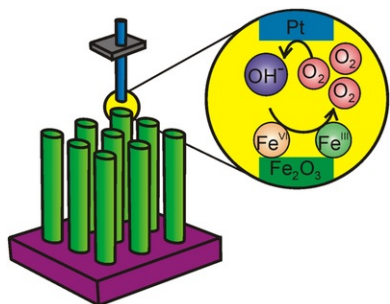
- [63] R.H. Wood, The heat, free energy, entropy of the ferrate(VI) ion, *J. Am. Chem. Soc.* **80**, 1958, 2038.
- [64] D.G. Lee and H. Gai, Kinetics and mechanism of the oxidation of alcohols by ferrate ion, *Can. J. Chem.* **71**, 1993, 1394.
- [65] R.J. Audette, J.W. Quail, W.H. Black and B.E. Robertson, Crystal structures of  $M_2FeO_4$  (M = potassium, rubidium, cesium), *J. Solid State Chem.* **8**, 1973, 43.
- [66] Y.D. Perfiliev and V.K. Sharma, Higher oxidation states of iron in solid state: synthesis and their Mossbauer characterization, *ACS Symp. Ser.* **985**, 2008, 112.
- [67] K. Bouzek, I. Rousar, H. Bergmann and K. Hertwig, The cyclic voltammetric study of ferrate(VI) production, *J. Electroanal. Chem.* **425**, 1997, 125.
- [68] Y. Shen, M. Träuble and G. Wittstock, Detection of Hydrogen Peroxide Produced during Electrochemical Oxygen Reduction Using Scanning Electrochemical Microscopy, *Anal. Chem.* **80**, 2008, 750.
- [69] K. Eckhard, X. Chen, F. Turcu and W. Schuhmann, Redox competition mode of scanning electrochemical microscopy (RC-SECM) for visualisation of local catalytic activity, *Phys. Chem. Chem. Phys.* **8**, 2006, 5359.
- [70] W. Nogala, M. Burchardt, M. Opallo, J. Rogalski and G. Wittstock, Scanning electrochemical microscopy study of laccase within a sol-gel processed silicate film, *Bioelectrochemistry* **72**, 2008, 174.
- [71] J.O. Bockris and T. Otagawa, The electrocatalysis of oxygen evolution on perovskites, *J. Electrochem. Soc.* **131**, 1984, 290.
- [72] P. Paredes Olivera, E.M. Patrito and H. Sellers, Hydrogen peroxide synthesis over metallic catalysts, *Surf. Sci.* **313**, 1994, 25.
- [73] K. Juodkazis, J. Juodkazyte, R. Vilkauskaitė and V. Jasulaitienė, Nickel surface anodic oxidation and electrocatalysis of oxygen evolution, *J. Solid State Electrochem.* **12**, 2008, 1469.
- [74] M.E. Abdelsalam, G. Denuault, M.A. Baldo, C. Bragato and S. Daniele, Detection of Hydroxide Ions in Aqueous Solutions by Steady-State Voltammetry, *Electroanalysis* **13**, 2001, 289.
- [75] M.E. Abdelsalam, G. Denuault, M.A. Baldo and S. Daniele, Voltammetry of hydroxide ion in aqueous solutions on gold microelectrodes, *J. Electroanal. Chem.* **449**, 1998, 5.
- [76] S. Daniele, M.A. Baldo, C. Bragato, G. Denuault and M.E. Abdelsalam, Steady-State Voltammetry for Hydroxide Ion Oxidation in Aqueous Solutions in the Absence of and with Varying Concentrations of Supporting Electrolyte, *Anal. Chem.* **71**, 1999, 811.
- [77] B. Liu and A.J. Bard, Scanning Electrochemical Microscopy. 45. Study of the Kinetics of Oxygen Reduction on Platinum with Potential Programming of the Tip, *J. Phys. Chem. B* **106**, 2002, 12801.

## Appendix A. Supplementary data

The following are Supplementary data to this article:

[Multimedia Component 1](#)

### Graphical abstract



---

## Highlights

- Nanostructured Pt microelectrode as highly sensitive and stable O<sub>2</sub> sensor in SECM.
  - Identification of new surface redox transitions in nanostructured iron oxide electrodes.
  - Identification of O<sub>2</sub> released during surface redox transitions in iron oxide thin films. [\[bullet point\] Likely involvement of Fe III/VI redox transition in OER in alkaline solution.](#)
- 

## Queries and Answers

**Query:** The author names have been tagged as given names and surnames (surnames are highlighted in teal color). Please confirm if they have been identified correctly.

**Answer:** Author surnames are identified correctly

**Query:** Please check that the affiliations link the authors with their correct departments, institutions, and locations, and correct if necessary.

**Answer:** institutions are corrected for Dosche

**Query:** Please check the e-mail addresses for all the authors and correct if necessary.

**Answer:** email addresses are correct

**Query:** Please note that two sets of highlights were provided. Therefore, one has been followed. Please check and amend if necessary.

**Answer:** This was the wrong set of highlights. The most recent must be used.

**Query:** “Your article is registered as a regular item and is being processed for inclusion in a regular issue of the journal. If this is NOT correct and your article belongs to a Special Issue/Collection please contact a.elumalai@elsevier.com immediately prior to returning your corrections.”

**Answer:** The article is for a regular issue